Catalysis Science & Technology

ROYAL SOCIETY OF CHEMISTRY

PAPER

View Article Online
View Journal | View Issue

Cite this: *Catal. Sci. Technol.*, 2021, **11**, 3141

Rational design of interface refining through Ti^{4+}/Zr^{4+} diffusion/doping and TiO_2/ZrO_2 surface crowning of $ZnFe_2O_4$ nanocorals for photoelectrochemical water splitting†

Sarang Kim,‡[a] Mahadeo A. Mahadik,‡[a] Anushkkaran Periyasamy,[a] Weon-Sik Chae,[b] Jungho Ryu,[c] Sun Hee Choi *[d] and Jum Suk Jang *[a]

Received 23rd November 2020,
Accepted 28th February 2021

DOI: 10.1039/d0cy02255a

rsc.li/catalysis

The development of advanced assemblies of interfacial under- and overlayered photoanodes is an effective technique to overcome the problem of slow charge separation and enhance solar energy conversion. The present study reports *in situ* zirconium-doped zinc ferrite nanocorals (Zr-ZFO NCs) and introduces the concept of diffusion/doping and surface passivation using a TiO_2 underlayer *via* quenching. The high-temperature quenching aids the Zr doping/Ti^{4+} diffusion in the bulk and, at the same time, the ZrO_2/TiO_2 composite layers passivate the surface of ZFO NC photoanodes. The optimum TiO_2-underlayer-modified Zr-ZFO (TZF) photoanode shows a dramatically improved photocurrent (0.48 mA cm^{-2}) at 1.23 V *vs.* RHE, which is twice that of the bare Zr-ZFO. Further, the addition of an Al_2O_3/CoO_x cocatalyst further accelerates the surface reaction kinetics of the TZF, and significantly improved charge separation efficiency, photocurrent density (0.73 mA cm^{-2} at 1.23 V *vs.* RHE; and 0.97 mA cm^{-2} at 1.4 V *vs.* RHE), and stability were obtained. Compared to conventional ZFO nanorods (0.14 mA cm^{-2} at 1.23 V *vs.* RHE), the optimized sample shows a 421% increase in photocurrent density. Additionally, the TZF/Al_2O_3/CoO_x–1 mM photoanode generates 65 and 130 μmol oxygen and hydrogen, respectively, under simulated 1 sun illumination. Thus, the "sandwich" strategy for Zr-ZFO with a TiO_2 underlayer and spontaneous surface passivation *via* quenching could be expanded for the design and fabrication of many low-efficiency photocatalysts and the production of cost-effective PEC water splitting photoelectrodes.

1. Introduction

The fast growth of the industry and global population has resulted in several serious issues, such as energy depletion and environmental pollution. Therefore, the search for clean and sustainable energy resources is of paramount importance. The use of solar energy to produce chemical fuels from water *via* splitting of water is considered one of the "Holy Grails of modern science".[1] Since the revolutionary discovery by Honda and Fujishima of photoelectrochemical (PEC) water splitting over TiO_2 under UV illumination to produce hydrogen,[2] extensive efforts have been made to develop novel semiconductors; in particular, the alteration of bandgap and surface engineering have been exploited to improve the catalytic and photoelectrocatalytic performances towards splitting of water.[3–5] Improving the surface area for absorption of light and the photoelectric properties and nanostructuring the material architecture are some of the most effective approaches for improving the photocatalytic performance.[6] Hematite (α-Fe_2O_3) is one of the capable candidates that meets many of the water oxidation half-reaction requirements, but its short hole diffusion length (2–4 nm) and unsatisfactory conductivity reduce its photoelectrochemical performance.[7] Of the metal oxides, spinel zinc ferrite ($ZnFe_2O_4$, ZFO) represents an attractive class of ternary metal oxides and is a capable material for PEC splitting of water as it has a narrow bandgap (2.0 eV) which permits the use of a large amount of the solar spectrum; in addition, it shows a low onset potential, has high photochemical stability and is low cost.[8] However, the

[a] *Division of Biotechnology, Advanced Institute of Environmental and Bioscience, College of Environmental and Bioresource Sciences, Chonbuk National University, Iksan 570-752, Republic of Korea. E-mail: jangjs75@jbnu.ac.kr*
[b] *Daegu Center, Korea Basic Science Institute, Daegu 41566, Republic of Korea*
[c] *Geologic Environment Research Division, Korea Institute of Geoscience and Mineral Resources (KIGAM), Daejeon 305-350, Republic of Korea*
[d] *Pohang Accelerator Laboratory (PAL), Pohang University of Science and Technology (POSTECH), Pohang 790-784, Republic of Korea. E-mail: shchoi@postech.ac.kr*

† Electronic supplementary information (ESI) available: UV-vis absorbance and Tauc plots, XPS, *J–V*, EIS, IPCE, ABPE, IMPS. See DOI: 10.1039/d0cy02255a

‡ Authors with equal contribution.

poor conductivity and sluggish water oxidation kinetics of ZFO are the main barriers for its use in water splitting as well as in supercapacitors.[9,10] To date, reports concerning the investigation of water photooxidation on bare $ZnFe_2O_4$ are scant.[11,12] Recently, the successful realization of the ion doping method has been used to solve the poor electrical conductivity and fast electron and hole recombination in $ZnFe_2O_4$.[13] For example, $ZnFe_2O_4$ materials doped with a heteroatom, such as Mn, Ni, Ag *etc.*, are advantageous for boosting electronic conductivity.[14–16] Lee *et al.* also incorporated the tetravalent Ti^{4+} and Sn^{4+} cations into Fe^{3+} sites of $ZnFe_2O_4$ under consecutive annealing at 550 and 800 °C or hybrid microwave annealing.[17]

Among the dopants, Ti doping results in a substantial improvement in the photoelectrochemical performance of zinc ferrite. Guo *et al.* also reported that Ti^{4+}-doped $ZnFe_2O_4$ exhibits 8.75 times higher photocurrent density (0.35 mA cm^{-2} at 1.23 V *vs.* RHE) compared to the pure $ZnFe_2O_4$.[18] However, the present value is still far smaller than the theoretical value of ≈11 mA cm^{-2} reported for ZFO.[19] In addition to doping, the use of underlayers and overlayers is a fruitful way to advance the conductivity of materials.[20] Previous studies have used metal oxides such as Ga_2O_3,[21] SiO_x,[22] Nb_2O_5,[23] and TiO_2 (ref. 15) as model systems to investigate the use of underlayers for improving the photoelectrochemical capacity of electrodes. These oxide underlayers suppress electron recombination from the fluorine-doped tin oxide (FTO) substrate to the hematite thin films. Therefore, it could be convenient to fabricate rational integration of interfacial under-and overlayers for improving the photoelectrochemical capacity of $ZnFe_2O_4$ photoanodes. However, to date, there have been no reports on $ZnFe_2O_4$ NCs grown on spin-coated TiO_2 underlayers and none have been treated with high-temperature quenching to achieve controlled Zr/Ti diffusion/doping and surface passivation using induced elemental diffusion from the underlayer.

In this work, we report the influence of the TiO_2 underlayer on the synthesis and PEC performance of *in situ* diluted hydrothermally prepared Zr-doped $ZnFe_2O_4$ NC photoanodes. Our approach of *in situ* generation of $ZnFe_2O_4$ nanocoral framework on spin-coated TiO_2 underlayer/FTO through an *in situ* diluted hydrothermal method is significantly exclusive, unlike the other conventional $ZnFe_2O_4$ synthesis approaches.[11,12,24,25] The influence of high-temperature quenching on the trade-off between the diffusion/doping and ZrO_2/TiO_2 surface passivation of $ZnFe_2O_4$ and the charge separation efficiencies of $ZnFe_2O_4$ was investigated. The optimized TiO_2 underlayers suppress both bulk and surface charge carrier recombination and facilitate charge transportation from the Zr-ZFO NC photoanodes to FTO *via* diffusion. Moreover, we applied duel modification strategies to enhance the hole transfer kinetics at the semiconductor–electrolyte interface, *i.e.* Al_2O_3 surface passivation layer and cobalt oxide (CoO_x) oxidation cocatalyst loading. These optimization strategies led to excellent PEC water splitting activity with a 0.78 V *vs.* RHE cathodically shifted onset potential and photocurrent density of 0.73 mA cm^{-2} at 1.23 V *vs.* RHE. Compared to conventional ZFO nanorods (0.14 mA cm^{-2} at 1.23 V *vs.* RHE), the optimized sample shows a 421% increase in photocurrent density. We believe that our synthetic strategies could be used for other small-bandgap multinary ferrites and ferroelectric photoanodes that have poor charge transport characteristics.

2. Experimental

2.1 Deposition of TiO_2 underlayers

Titanium diisopropoxide bis(acetylacetonate) was mixed with ethanol to prepare 5, 15 and 45 mM solutions for the spin-coating. Then, ultrasonically cleaned FTO was used as a substrate and 75 μl solution was spin-coated on FTO at the rate of 1500 rpm for 30 s. Further, the as-synthesized films were quenched in a box furnace at 400 °C for 30 min. The TiO_2 underlayer thickness on the FTO surface was easily controlled by the dilution of titanium diisopropoxide bis(acetylacetonate) with ethanol from 5, 15 and 45 mM. Depending on the Ti precursor concentrations, the samples with TiO_2 underlayer were denoted as TZF-5, TZF-15, and TZF-45, respectively.

2.2 Preparation of the Zr-doped zinc ferrite on TiO_2 underlayer

The as-deposited TiO_2 underlayer/FTO glass substrates were placed vertically in a vial with the conducting edge facing towards the wall. Further, a 20 ml vial was filled with 10 ml of an aqueous solution of 4.6 mM $FeCl_3{\cdot}6H_2O$ and 1.0 M $NaNO_3$ (pH 1.5). Then, one ml of 4.1336 μl/10 ml $ZrO(NO_3)_2$/ethanol solution was further added to the hydrothermal synthesis precursor solution. Furthermore, these vials were kept in an electric oven for 6 h at 100 °C. After the reaction, the Zr-doped akaganéite (Zr–FeOOH) films were deposited on FTO substrate, which was again rinsed with distilled water. In the second step, a 150 μl ethanol solution of 20 mM $Zn(NO_3)_2$ was added dropwise onto hydrothermally prepared Zr–FeOOH nanostructured films. Then, the as-prepared photoanodes were dried in an electric oven for 45 min at 35 °C. Next, these Zn-dropped/Zr–FeOOH films were first quenched at 800 °C for 13 min to transform into the ZnO/Zr-ZFO photoanode. In order to eradicate the spare ZnO layer on the surface of ZnO/Zr-ZFO, the electrodes were steeped in 1 M NaOH aqueous solution (12 h with constant stirring). Thereafter the electrodes were further quenched at 820 °C for 15 min. These synthesized $ZnFe_2O_4$ photoanodes were denoted as TZF.

2.3 Passivation overlayer with Al_2O_3 treatment and surface modification

Surface treatment of optimized TZF photoanodes was carried out by slight modification of our previous method.[26] Optimized TZF films were dipped in 10 mM aluminum chloride in ethanol solution for 2 min. The films were annealed at 200 °C/30 min for the development of an amorphous overlayer. This photoanode was named TZF/Al_2O_3. Further, CoO_x amorphous overlayer was coated on the TZF/Al_2O_3 photoanode by spin-

coating. Cobalt acetate tetrahydrates were dissolved in water to form 0.5, 1, 5 mM solutions. The solutions were coated on the surface of the sample treated with aluminum for 25 s and 2500 rpm. Lastly, the cobalt acetate coated photoanodes underwent heat treatment of 250 °C for 15 min. These photoanodes were denoted as TZF/Al_2O_3/CoO_x_0.5 mM, TZF/Al_2O_3/CoO_x_1 mM and TZF/Al_2O_3/CoO_x_5 mM.

2.4 Characterization

The morphology and microstructure of the TZF-based photoanodes were studied using a field emission scanning electron microscope (FESEM, ZEISS SUPRA 40VP). Further, transmission electron microscopy (TEM) micrographs and elemental mapping of the as-prepared photoanodes were obtained through a JEOL ARM-200F instrument. X-ray photoelectron spectra (XPS) of the TZF-based photoanodes were measured using a PHI Quantera II spectrometer with monochromatic AlK_α X-ray source ($h\nu$ = 1486.6 eV, 25 W, and 15 kV). X-ray diffraction (XRD) patterns of the TZF-based photoanodes were identified using a PANalytical X'pert Pro MPD diffractometer with Ni-filtered Cu-K_α radiation (wavelength $K_{\alpha1}$ = 1.540598 Å and $K_{\alpha2}$ = 1.544426 Å). The optical properties of TZF-based photoanodes were recorded using a Shimadzu UV-vis spectrophotometer (UV-2600). The corresponding bandgap energies were calculated by the Tauc plot method:[27]

$$(\alpha h\nu)^{1/n} = A(h\nu - E_g) \quad (1)$$

where α, A and h are the absorption coefficient, proportionality constant and Planck's constant, respectively; ν indicates the photon frequency; the value of exponent n is dependent on the electronic transitions (n = 2 for indirect transitions); and E_g is the bandgap. X-ray absorption fine structure (XAFS) analyses were carried out using the 7D beamline of Pohang Accelerator Laboratory (PLS-II, linac energy: 3.0 GeV, storage ring current: 360 mA top-up). A Si (111) double crystal monochromator was utilized and the Fe K-edge (E_0 = 7112 eV) spectra were measured in fluorescence mode. The spectra were normalized and Fourier-transformed using ATHENA in the IFEFFIT suite of programs.[28] Time-resolved PL analysis was carried out using a confocal microscope (MicroTime-200, PicoQuant, Germany) with a UPLSAPO 40× super-apochromat objective. The excitation source was a pulsed diode laser (379 nm with 30 ps pulse width and 100 μW laser power), and emitted photons were detected by a PDM series, MPD avalanche photodiode and a time-correlated single-photon counting system (PicoHarp 300, PicoQuant GmbH, Germany). Exponential fitting of PL spectra was accomplished by iterative least-squares deconvolution fitting by the Symphotime-64 software (ver. 2.2) as follows,[29]

$$I(t) = \sum A_i e^{-t/\tau_i} \quad (2)$$

where $I(t)$, A, and τ are the PL intensity as a function of time, amplitude and the PL lifetime, respectively, and value of i is 2. The amplitude-weighted average lifetime ($\langle\tau\rangle$) is calculated by

$$\langle\tau\rangle = \sum A_i\tau_i^2 / \sum A_i\tau_i \quad (3)$$

2.5 Photoelectrochemical measurements

PEC analyses were carried out in a three-armed PEC reactor, where the ZFO-based photoanodes act as the working electrode, a Pt wire as the counter electrode, and Hg/HgO as the reference electrode. A 1 M NaOH (pH 13.6) aqueous solution was used as the electrolyte. An electrode area (1 × 1 cm^2) was kept constant during the PEC measurements. Photocurrent density *vs.* potential and photocurrent density *vs.* time curves were measured using an Ivium CompactStat potentiostat. The photoanodes were illuminated from the front side with light intensity to 100 mW cm^{-2} (1 sun illumination) using a 300 W xenon arc lamp (CEL-HXF 300, $320 < \lambda < 780$ nm). The measured potentials were converted against the reversible hydrogen electrode (RHE) using the Nernst equation.[30]

$$E_{RHE} = E_{Hg/HgCl} + 0.059\ pH + E^{\circ}_{Hg/HgCl} \quad (4)$$

$$\left(E^{\circ}_{Hg/HgCl} = 0.095\ V\ vs.\ NHE\ at\ 25\ ^{\circ}C\right)$$

where E *vs.* RHE is the potential *vs.* RHE and $E^{\circ}_{Hg/HgO}$ is the Hg/HgO reference electrode potential *vs.* NHE at 25 °C for the Hg/HgO/0.1 M NaOH. Electrochemical impedance spectroscopy (EIS) analyses were carried out at 1.23 V *vs.* RHE under 1 sun illumination and 3000 kHz to 0.5 Hz frequency range. Further, the experimental EIS data were fitted using the ZView (Scribner Associates Inc.) program. PEC water splitting was measured over the TZF/Al_2O_3/CoO_x electrode using a PEC water splitting cell reported in the literature.[31] The PEC water splitting reactor consists of TZF/Al_2O_3/CoO_x as the working electrode, a Pt wire counter electrode, and a Hg/HgO reference electrode. A 1 M NaOH (pH ≈ 13.6) aqueous solution was used as an electrolyte and 1.23 V *vs.* RHE was used as the applied potential. In order to remove dissolved oxygen from the electrolyte, the solution was purged with 99.9% nitrogen gas for 2 h before the start of the PEC water splitting experiments. The evolved hydrogen and oxygen during the PEC measurements at the Pt electrode and the TZF/Al_2O_3/CoO_x_1 mM photoanode were analyzed using a gas chromatograph (GC) with a thermal conductivity detector (GC-TCD, Agilent 7820, U.S.A.), a molecular sieve 5 Å column, and Ar carrier gas.

3. Results and discussion

The schematic process of the preparation of TZF photoanode is shown in Fig. 1A. As shown in Fig. 1A, the *in situ* Zr-doped ZFO NCs were hydrothermally synthesized on the TiO_2-modified FTO substrate. Subsequently, the $Zn(NO_3)_2$ precursor was added dropwise to the Zr-ZFO NCs followed by etching in 1 M NaOH for 12 h and quenching at 820 °C in air for 15 min to obtain a balance between the Zr/Ti diffusion/

doping and ZrO_2/TiO_2 surface passivation. The surface and cross-sectional FESEM images of Zr-ZFO with and without the TiO_2 underlayer substrates reveal that the Zr-ZFO/TiO_2 photoanode consists of numerous NC structures with width and length of ≈185 nm and 420 nm, respectively (Fig. 1B and C). The microstructure and chemical composition of a selected area of the optimized TZF (TZF-15, *i.e.*, TiO_2 underlayer prepared with a 15 mM precursor solution) photoanode were analyzed using HRTEM and scanning TEM energy-dispersive X-ray (STEM-EDX) analyses. Fig. 1D shows the bright-field TEM image of the cross-sectional specimen obtained using the focused ion beam (FIB) technique. The HRTEM image (Fig. 1E) reveals distinct lattice fringes with an interplanar spacing of 2.98 Å, which agrees with the *d*-spacing of the (220) plane of ZFO. The corresponding reduced fast Fourier transform (FFT) pattern is shown in the inset of Fig. 1E, suggesting the formation of pure $ZnFe_2O_4$. Further, Fig. 1F shows the energy dispersive X-ray spectroscopy (EDS) spectra taken at three different positions on the TZF-15 photoanode, which clearly indicate that Ti diffusion occurred from the underlayer to the top of the Zr-ZFO. Spectra 1 and 2 were taken from the top and the middle point of the TZF-15 NCs, respectively, and indicate Ti contents of 0.19 and 0.24 wt%, respectively. Surprisingly, after high-temperature quenching, a small amount (0.04 wt%) of Ti ions was present on the surface of the TZF-15 NC (spectrum 3), confirming that the Ti ions that diffused from the TiO_2 underlayer had reached the top of the Zr-ZFO samples. Furthermore, EDS elemental mapping (Fig. 1G) revealed that Zn, Fe, and O were homogeneously dispersed over the samples, whereas the presence of small quantities of Zr, Sn, and Ti at expected positions confirm the Zr-doping and Ti and Sn diffusion. Moreover, the FIB-TEM analysis results suggest that the formation of the TiO_2 underlayer on FTO substrates is an effective method for achieving Ti diffusion in the Zr-ZFO photoanodes. Additionally, to confirm the presence of the TiO_2 layer on the FTO, the point EDS spectra of FIB-TEM cross-sectional micrographs of the TZF-15 photoanode were recorded, as shown in Fig. S1,† The EDS spectra reveal the wt% compositions of Fe, O, Zn, Zr, Ti, and Sn elements in the sample at different points. Spectrum 5 taken from the FTO substrate part of photoanodes shows 0.0 wt% Ti with higher Sn wt%, whereas spectrum 4 and spectrum 6 collected near the TiO_2/FTO surface indicate the higher wt% of Ti. This confirms the presence of a TiO_2 layer on the FTO substrate. Furthermore, spectrum 9 collected from the bulk of TZF-15 shows a lower wt% (0.2 wt%) than spectrum 4. Interestingly on the surface of TZF-15, the EDS spectrum collected at points (spectrum 10 and spectrum 11) clearly indicates the formation of a nonuniform TiO_2 layer after quenching at 820 °C for 15 min. A TEM-EDS line profile obtained from the cross section of the TZF-15 NC photoanode further reveals the diffusion/doping of Ti (Fig. S2(a–c)).† Thus, the EDS spectra and corresponding TEM line profile gained from TEM-EDS analysis reveal the presence of Fe, O, Zn, Zr, Ti, and Sn elements in the sample. Fig. 2A shows an X-ray diffraction pattern containing reflections at 30°, 35.2°, and 42.8°, which resemble the (220), (311), and (400) lattice planes of cubic structured spinel ZFO ($ZnFe_2O_4$: JCPDS no. 89-4926). The other X-ray diffraction peaks can be indexed to the FTO substrate (as indicated by "●," JCPDS no. 41-1445). There are no other crystalline impurity peaks related to TiO_2 or elemental Ti. This is either because the low amount of TiO_2 or because the Ti dopant did not diffuse sufficiently homogeneously to be measured. Additionally, there are no peaks corresponding to akaganeite or ZnO, indicating that the ZFO was perfectly synthesized after the etching and quenching process. As shown in Fig. S3,† the absorption edges of the Zr-ZFO and TZF samples were at around 620 nm, and their calculated bandgaps (E_g) are both 2.02 eV. XPS analysis was used to confirm the Zr and Ti diffusion as well as the composition of the TZF-15 photoanode after the high-temperature quenching. As shown in Fig. 2(B), the Zr 3d spectrum exhibits the spin-orbit doublet Zr $3d_{5/2}$–Zr $3d_{3/2}$ for the Zr-ZFO, TZF-15, and TZF-45 photoanodes. The binding energy (BE) values of Zr $3d_{5/2}$ and Zr $3d_{3/2}$ of Zr-ZFO are positioned at 181.8 eV and 184.3 eV, which is consistent with that of Zr in the 4+ state (ZrO_2: Zr $3d_{5/2}$ (182.0 eV) and Zr $3d_{3/2}$ (184.4 eV)).[32,33] However, the binding energy values of TZF-15 and TZF-45 are positioned at 181.8 eV (Zr $3d_{5/2}$) and 184.0 eV (Zr $3d_{3/2}$), which are 0.3 eV

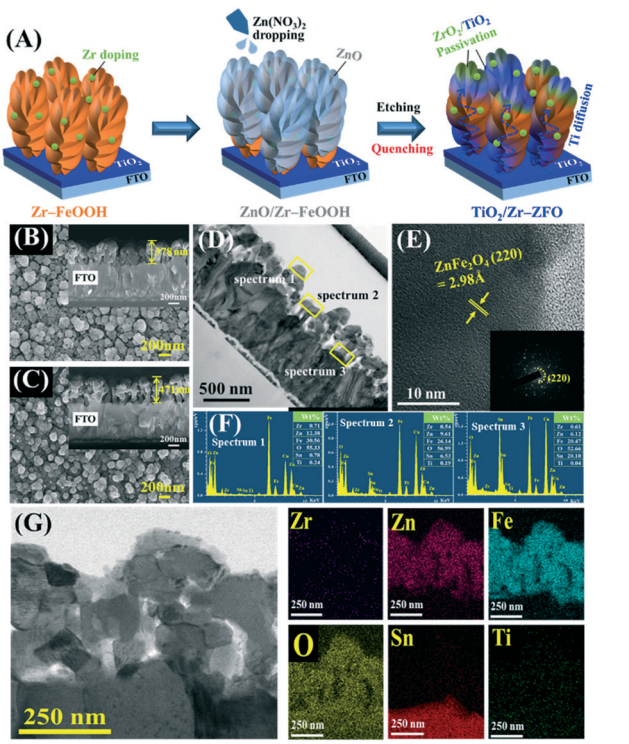

Fig. 1 (A) Schematics of the TZF NC photoanode synthesis process. FESEM top and cross-sectional views (inset) of (B) Zr-ZFO and (C) TZF-15. (D) Low-magnification TEM images, (E) HR-TEM image (the inset shows the corresponding FFT pattern), (F) three-point EDS spectra revealing the weight percentage (wt%) compositions of Zr, Zn, Fe, O, Sn, and Ti, and (G) EDS elemental mapping of TZF-15 photoanode obtained using a focused ion beam (FIB).

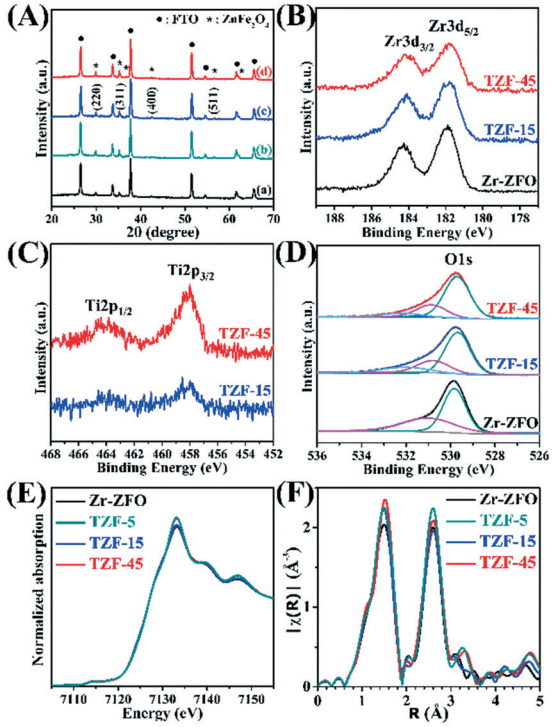

Fig. 2 (A) XRD patterns and narrow scan XPS spectra of (B) Zr 3d, (C) Ti 2p, and (D) O 1s. (E) XANES spectra and (F) Fourier transforms of k^2-weighted EXAFS functions for the Fe K-edges of (a) Zr-ZFO, (b) TZF-5, (c) TZF-15, and (d) TZF-45 photoanodes.

negative shifts compared with that of Zr-ZFO (Zr $3d_{3/2}$). The negative shift in (Zr $3d_{3/2}$) binding energies suggests that some zirconium ions in Zr^{4+} doped ZFO tend to get electrons. Further, as shown in Fig. 2C, the binding energies of the Ti $2p_{3/2}$ peak of TZF-15 and TZF-45 photoanodes are 457.8 eV and 458.2 eV, respectively, implying that Ti cations are in slightly different atomic environments in the two samples. The redshift is comparable to that of a pure TiO_2 sample (458.5 eV),[34] which suggests that Ti ions are indeed diffused/doped into the ZFO lattices. Cao *et al.* also reported that the presence of Ti $2p_{3/2}$ and Ti $2p_{1/2}$ XPS peaks at binding energies of 458.1 eV and 464.1 eV are representative of the presence of Ti^{4+} on the hematite photoanode.[35] However, as the precursor concentration of the TiO_2 underlayer increased from 15 to 45 mM in the TZF sample, the intensity of the Ti $2p_{3/2}$ peak increased with the shift in the binding energy to that of the TZF-15. This is due to the increased Ti diffusion from the TiO_2 underlayer towards the surface of ZFO with increasing initial Ti precursor concentration. In addition, the atomic ratios of Ti : Fe and Zr : Fe obtained from the XPS quantitative analysis of optimized TZF-15 were 0.05% and 0.28%, respectively. The above results indicate that Ti and Zr elements have successfully co-doped/diffused into the ZFO photoanode. Thus, after 820 °C quenching, the Ti atoms diffused from the TiO_2 underlayer towards the Zr-ZFO NC's surface, thus forming a passivation layer on the surface of Zr-ZFO. However, the passivation layer becomes thicker at the higher Ti precursor concentrations because of the relatively large number of Ti atoms diffused from the TiO_2 underlayer to the photoanode's surface. As shown in Fig. S4A,† the XPS Zn 2p spectra exhibit two peaks at BEs of 1020.9 and 1043.9 eV which are ascribed to Zn $2p_{3/2}$ and Zn $2p_{1/2}$, respectively. This confirms that the zinc is in the 2+ oxidation state and agrees with the reported ZFO values.[11,36] The Fe 2p XPS spectra (Fig. S4B†) show the presence of two peaks at BEs of 724.9 and 710.9 eV which corresponds to Fe $2p_{1/2}$ and Fe $2p_{3/2}$, respectively. In addition to two main peaks, the presence of shake-up satellite peaks suggests the presence of the Fe^{3+} state.[37] As shown in Fig. 2D, a broad O 1s peak is located at around 529.8–532.0 eV. The O 1s peak was fitted to three constituent peaks, revealing three kinds of oxygen species.[38,39] The peak at 529.9 eV could be allocated to the lattice oxygen bound to Zn or Fe and the peak located at around 530.9 eV confirmed the presence of oxygen vacancies after the substitution of the Fe^{3+} sites with Ti^{4+}, whereas the peak at around 532 eV could be attributed to the coordination of H_2O or surface-absorbed O species.[40,41]

The local structure around Fe in the Zr-ZFO photoanodes with TiO_2 underlayers was examined by XAFS. The Fe K-edge X-ray absorption near-edge structure (XANES) spectra in Fig. 2E demonstrate that both TZF-5 and TZF-45 photoanodes have noticeably increased intensities for the resonance peaks at approximately 7140 and 7147 eV as well as for the absorption peak at 7133 eV compared to the non-TiO_2 underlayer sample. However, the spectrum for the 15 mM sample exhibits little difference. Because the absorption at the Fe K-edge is correlated to an electronic transition from the 1 s core level to the unoccupied p-states, the observed changes indicate that the Fe in the 45 mM samples becomes electron-deficient, whereas the Fe in the 15 mM sample preserves its closed electronic structure, as for Fe^{3+} in the sample without a TiO_2 underlayer. In addition, the presence of two separate peaks appearing in the Fe K-edge EXAFS spectra is shown in Fig. 2F. The first peak at 0.6–1.9 Å is due to the nearest Fe–O bonds, and the second shell-associated peak at 1.9–3.0 Å comprises the combined scattering for Fe–M (M = Fe, Zr, Ti, and Sn) bonds. The intensity of the Fe–O peak increases in the order 0 mM < 5 ≈ 15 mM < 45 mM TiO_2 precursor concentrations. With increasing TiO_2 precursor concentration, the increased thickness of the TiO_2 underlayer prevents the effective diffusion of Sn^{4+} from FTO into the Fe^{3+} lattice in hematite, resulting in increased Fe–O bond ordering.

To examine the role of the TiO_2 underlayer on the PEC activity of the Zr-ZFO NCs, the current density *vs.* potential (*J*–*V*) characteristics were systematically investigated under 1 sun illumination condition using 1 M NaOH solution as an electrolyte. The *J*–*V* curves for (a) FTO/pure ZFO, (b) FTO/TiO_2 (15 mM)/pure ZFO, (c) FTO/Zr-ZFO and (d) FTO/TiO_2 (15 mM)/Zr-ZFO photoelectrodes were obtained as shown in Fig. S5A.† In the case of the pure ZFO photoanode synthesised by dropping of 50 mM $Zn(NO_3)_2$/ethanolic solution onto the surface of β-FeOOH/TiO_2 underlayer films, the TiO_2 layer did not show any effect for the PEC performance of the ZFO photoanode. The photocurrent densities of FTO/TiO_2 (15 mM)/pure-ZFO (pure-ZFO with TiO_2 underlayer) and FTO/

pure-ZFO samples are similar, so they overlapped. However, all the TiO_2 underlayer deposited Zr-ZFO photoanodes show higher photocurrent density than that of solely Zr-ZFO (without TiO_2 underlayer) photoanodes, suggesting that the Ti^{4+} ion exhibits positive effects when the Zr^{4+} ion is present in the lattice of ZFO. EIS curves of FTO/TiO_2(15 mM)/pure-ZFO (pure-ZFO with TiO_2 underlayer) and FTO/pure-ZFO samples show that even though there is an increase in the R_{CT1} after the addition of the TiO_2 underlayer, the R_{CT2} value is decreased considerably (Fig. S5B and Table S1†). This is due to the different thickness of films and high Ti concentration that can prevent effective Sn and Ti doping/diffusion into the ZFO lattice. Fig. 3A shows *J–V* curves of Zr-ZFO and TZF series electrodes prepared using controlled concentrations of the TiO_2 precursor used to form the underlayers. Typically, the Zr-ZFO photoanodes achieved a photocurrent density of 0.23 mA cm^{-2} at 1.23 V *vs.* RHE with an onset potential of 1.01 V *vs.* RHE. After deposition of TiO_2 underlayer, the TZF-5 sample exhibited a photocurrent density of 0.37 mA cm^{-2} at 1.23 V *vs.* RHE with an onset potential of 0.94 V *vs.* RHE. Furthermore, when the concentration of the TiO_2 underlayer precursor was increased to 15 mM, the resultant TZF-15 photoanode yielded an enhanced photocurrent density of 0.48 mA cm^{-2} at 1.23 V *vs.* RHE (0.68 mA cm^{-2} at 1.4 V *vs.* RHE) which is twice than that of the Zr-ZFO photoanode. This steep slope in the photocurrent density curve indicates that the TZF-15 photoanode has a low electron–hole recombination rate. The increased slope of TZF-15 can be explained by the transfer of more electrons to the FTO substrate than in the other samples. Thus, the enhanced PEC performance of the TZF photoanodes is due to Ti^{4+} doping/diffusion into Zr-ZFO from the TiO_2 underlayer and the charge recombination suppression at the interface of the Zr-ZFO and FTO substrates. The improved performance of the TZF-15 compared to the other widely used Ti dopant is due to fact that Zr does not trap carriers in TZF-15 since Zr^{3+} is less stable than Ti^{3+}. Liao and co-workers reported that according to *ab initio* quantum mechanics calculations, the n-type zirconium dopant does not act as an electron trapping site due to the higher instability of Zr^{3+} and therefore can provide more charge carriers without inhibiting transport in the Zr–Ti co-doped/diffused ZFO in TZF-15 photoanodes.[42,43] Thus, Ti and Zr are considered to be special dopants owing to their facile and useful fabrication methods and the rapid charge separation rate. In a nutshell, the photocurrent density of the TZF photoanodes is strongly influenced by the Ti precursor concentration. *J–V* curves show that the Zr-ZFO grown on FTO with a TiO_2 underlayer exhibits a cathodic shift in the onset potential of TZF relative to that of the Zr-ZFO photoanodes. It is well known that a cathodic shift in the onset potential is related to passivation on the surface of the photoanodes.[35] However, as the Ti precursor concentrations were increased beyond 15 mM, the photocurrent density started to decrease, and the onset potential shifted to the anodic side. The TZF-45 photoanode shows an anodic shift

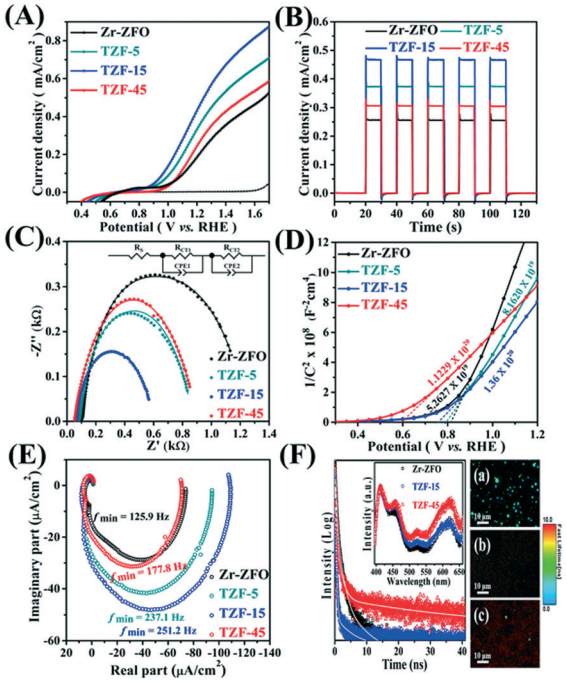

Fig. 3 (A) Photocurrent density *vs.* applied potential curves under 1 sun illumination (solid lines) and dark conditions (dashed lines). (B) Photocurrent–time plots with chopped light on/off cycles. (C) Nyquist plots measured at 1.23 V *vs.* RHE (under light). The inset shows the equivalent circuit for EIS fitting, (D) Mott–Schottky plots under dark conditions, (E) IMPS response of Zr-ZFO, TZF-5, TZF-15, and TZF-45 at 1.23 V *vs.* RHE (under light) using 1 M NaOH, (F) time-resolved PL decay and lifetime images of the Zr-ZFO, TZF-15, and TZF-45 photoanodes. The overlapped solid lines are simulated exponential fitting lines. The inset is the PL spectra of the corresponding photoanodes after 350 nm excitation. TRPL images of the corresponding PL decays of (a) Zr-ZFO, (b) TZF-15 and (c) TZF-45, which clearly present elongated PL lifetimes.

in the photocurrent onset and a notable decrease in the photocurrent density (0.28 mA cm^{-2} at 1.23 V *vs.* RHE). Possibly, the Ti^{4+} overlayer in excess may block the hole transport and results in lower PEC performance. Thus, a Ti^{4+} passivation layer can act as a TiO_x resistance layer. This hypothesis will be further explored using the electrochemical impedance spectroscopy (EIS) results shown in Fig. 3C.

Furthermore, to understand the role of the TiO_2 underlayer in the amended PEC performance, transient photocurrent responses of the photoanodes under chopped light were obtained, as shown in Fig. 3B. There are striking positive peaks for both Zr-ZFO and TZF, indicating that photogenerated holes are stored at the photoelectrode/electrolyte interface.[44] We further analyzed the Zr-ZFO and TZF series samples for long-term stability under 1 sun irradiation (Fig. S6A†) at 1.23 V *vs.* RHE. As a result, 99% stable photocurrent densities were achieved for the TZF samples, indicating that the NC structures did not decompose and were maintained during water oxidation. The results are well matched with the *J–V* results. To determine the photoresponse efficiency of Zr-ZFO and TZF series photoanodes, the applied bias photon-to-current efficiency

(ABPE) *vs.* applied potential was measured, as shown in Fig. S6B.† The ABPE is determined by the equation given below:[45]

$$\text{ABPE}\ (\%) = J \times (1.23 - V)/P \times 100 \quad (5)$$

where J, V and P are the photocurrent density under 1 sun illumination (mA cm^{-2}), applied potential and the power density of 100 mW cm^{-2}, respectively. A maximum ABPE value of 0.37% at 1.07 V *vs.* RHE was reached for TZF-15, which is 2.5 times that of Zr-ZFO. This is an outstanding result considering the contribution of both TiO_2/ZrO_2 surface passivation and Ti^{4+}/Zr^{4+} diffusion/doping to the PEC performance. To explain the advantages of the TiO_2 underlayer on the charge transfer process in the Zr-ZFO and TZF series photoanodes, EIS analyses were carried out at 1 sun illumination. Fig. 3C shows the Nyquist plots of Zr-ZFO and TZF series samples fitted using two resistor–capacitor (RC) equivalent circuits. EIS fitted parameters are given in Table 1. The EIS equivalent circuit consists of R_s which is the sheet resistance of the FTO substrates and R_{CT1} and R_{CT2} which indicate the charge transfer resistance in the bulk and photoanode/electrolyte interface, whereas CPE1 and CPE2 are the capacitance corresponding to R_{CT1} and R_{CT2}, respectively. It is apparent that the R_s value drops from 72 to 60 Ω as the TiO_2 precursor solution concentration increases. This phenomenon indicates that a thicker TiO_2 underlayer acts as a protective barrier against FTO deformation during the high-temperature quenching.[46,47] Thus, the conductivity of the FTO substrate was protected and R_s decreased. The TZF samples showed drastically decreased semicircle radii compared to those of the Zr-ZFO photoanode, indicating that the photogenerated holes at the interface of the electrode/electrolyte were dramatically reduced by the surface passivation with TiO_2/ZrO_2. Interestingly, both resistances (R_{CT1} and R_{CT2}) were reduced after the insertion of the TiO_2 layer on the FTO substrate, demonstrating a distinct enhancement in the charge separation.[48] Notably, the lower values of R_{CT1} after the addition of the TiO_2 underlayer in TZF-15 is owing to the suppressed electron–hole recombination at the FTO–photoanode interface and the large amount of Ti^{4+} diffusion from the underlayer to the Zr-ZFO NCs. In addition, the decreased value of R_{CT2} indicates that the diffused ZrO_2/TiO_2 acts as a passivating layer on the TZF photoanodes. This indicates the occurrence of Ti^{4+} diffusion/doping from the TiO_2 underlayer and the surface passivation of the TZF samples after quenching. The Mott–Schottky (MS) plots of the photoanodes were measured in the dark from 0.3 to 1.7 V *vs.* RHE at a constant applied frequency of 100 Hz; in this manner, the donor density (N_D) was assessed using the equation:[49]

$$N_D = (2/e_0\varepsilon\varepsilon_0)[d(1/C^2)dV]^{-1} \quad (6)$$

where e_0 is the electron charge (1.602×10^{-19} C), ε and ε_0 are the dielectric constant of zinc ferrite (80) and permittivity of vacuum (8.854×10^{-12} Fm^{-1}), whereas the capacitance (C) results from the electrochemical impedance. MS analysis shows the n-type semiconductor characteristics of the Zr-ZFO and TZF photoanodes (Fig. 3D). By extrapolating the x-intercepts of the linear region in the MS plots, the flat band potential (V_{FB}) values of the Zr-ZFO and TZF series photoanodes were obtained and were found to be cathodically shifted as the Ti concentration increased. During the high-temperature quenching process, Ti^{4+} ions diffused into the Zr-ZFO from the FTO substrates and TiO_2 underlayer, which caused an increase in the charge-carrier density than that of Zr-ZFO.[50] The higher doping in Zr-ZFO after treatment with the 45 mM TiO_2 precursor for underlayer formation is also consistent with the XPS analysis (Fig. 2C), where the TZF-45 photoanode showed a higher peak intensity corresponding to Ti because of the larger number of Ti ions that had diffused into the Zr-ZFO NC lattice. Fig. 3E shows the complex plane plots of the intensity-modulated photocurrent spectroscopy (IMPS) response for Zr-ZFO and TZF series photoanodes at 1.23 V *vs.* RHE. The IMPS measurements were performed in the 10 kHz to 0.1 Hz frequency range with a blue light-emitting diode (LED, peak wavelength 460 nm) driven by a frequency-response analyzer, and light intensities were modulated with a depth of 10%. The electron transport time (τ_d) was obtained using the value of the frequency at the bottom of the semicircle, calculated by the equation:[51]

$$\tau_d = 1/2\pi f_{min} \quad (7)$$

where f_{min} is the frequency of the minimum point in the IMPS semicircle. The calculated electron transport times of each sample are listed in Table S2.† The TZF-15 sample exhibits a shorter electron transport time of 634 μs than the other samples because of the optimized Ti^{4+} diffusion/doping, which further contributes to the smaller charge resistance and increased donor density of TZF-15 compared to those of the Zr-ZFO photoanodes.

For the photoanode materials, the photoluminescence (PL) emissions appear in the visible region, but there was a minor intensity modulation after the introduction of the TiO_2 underlayer (inset of Fig. 3F). To investigate the emission characteristics in more detail, we studied the time-resolved PL behavior after excitation with a 379 nm pulse laser. The Zr-ZFO on FTO showed three lifetime sub-components consisting of 0.3, 1.1, and 5.6 ns with an average lifetime of 0.47 ns. When the sample treated with the 15 mM TiO_2 underlayer precursor solution was used (TZF-15), the measured PL lifetime had two sub-components of 0.17 and 2.0 ns, as shown in Table S3.† In addition, the average lifetime was reduced to 0.21 ns, and the

Table 1 EIS fitting parameters for (a) Zr-ZFO, (b) TZF-5, (c) TZF-15 and (d) TZF-45 photoanodes measured at 1.23 V *vs.* RHE

Sample	R_S (Ω)	R_{CT1} (Ω)	R_{CT2} (Ω)	CPE1 (F)	CPE2 (F)
(a)	93	677	305	2.02×10^{-4}	2.94×10^{-5}
(b)	72	534	167	1.81×10^{-4}	3.61×10^{-5}
(c)	65	410	120	1.59×10^{-4}	4.48×10^{-5}
(d)	60	580	224	8.37×10^{-5}	4.41×10^{-5}

PL intensity was considerably quenched, as shown in Fig. 3F. With more TiO_2 (45 mM), interestingly, the PL decay could be fitted by three sub-components consisting of 0.23, 1.2, and 30 ns. The longest lifetime component (τ_3) was responsible for the increased average lifetime (0.62 ns). On the basis of the photocurrent measurements, the TZF-15 sample showed the best photon–current conversion activity. Considering the fast recombination and largely reduced emission intensity, this electrode might contain fast pathways for charge transport while reducing emissive recombination and, eventually, facilitating the PEC reaction. However, when the 45 mM TiO_2 precursor was used, the resultant thick TiO_2 underlayer did not have a positive effect because of the enlarged intrinsic carrier recombination property of the coated TiO_2 phase. An extraordinarily long lifetime is a well-known characteristic of TiO_2.[52] In this photoanode with a thick TiO_2 underlayer (TZF-45), the heterostructure does not produce the unique structural advantage for the PEC reaction. Thus, the PL results confirm that the incorporation of Ti and the formation of a ZrO_2/TiO_2 passivation layer of ZFO NC is important for extending the charge carrier lifetime and inhibiting electron–hole pair recombination in the photoelectrode.

To improve the surface charge separation properties and the kinetics of hole transfer at the surface of the ZFO photoanodes further, Al_2O_3 and CoO_x layers were deposited on the surface of the TZF-15 photoanode as a hole storage layer and oxygen evolution co-catalyst, respectively. To confirm the presence of the Al_2O_3 and CoO_x layers used for surface passivation on the TZF-15 and TZF/Al_2O_3/CoO_x_1 mM photoanodes, XPS analysis was carried out. Fig. 4A–D show the high-resolution Co 2p, Al 2p, O 1s, and Ti 2p XPS spectra for the TZF and TZF/Al_2O_3/CoO_x_1 mM photoanodes. In addition, Table S4† lists the atomic percentages of each element in the TZF and TZF/Al_2O_3/CoO_x_1 mM samples. The high-resolution XPS Co 2p spectrum of TZF/Al_2O_3/CoO_x_1 mM comprises two main peaks at BEs of 781.15 eV (Co $2p_{3/2}$) and 796.5 eV (Co $2p_{1/2}$) and satellite peaks at BEs of 786.7 and 802.3 eV.[28] In Fig. 4B, an Al 2p peak at a BE of 74.1 eV is present, and this corresponds to Al^{3+} for Al_2O_3 (typical value >74 eV),[53] confirming that Al_2O_3 was present in the TZF/Al_2O_3/CoO_x photoanodes. Fig. 4C shows the deconvolution of the O 1s spectra for the TZF and TZF/Al_2O_3/CoO_x_1 mM photoanodes. There are three peaks at binding energies in the range 529.8–532 eV. The major peak at 529.8 eV can be attributed to the lattice O species bound with metal ions such as Fe and Zn in the ZFO NCs. The central peak with a BE of 530.9 eV was allocated to oxygen vacancies and Co or Al–O, and the BE peak at 532 eV could be attributed to the coordination of H_2O or surface-absorbed O species (adsorbed OH^-).[54] Comparing the binding energies of both samples, there is a slight difference in the two peaks. The O 1s atomic percentage in the TZF/Al_2O_3/CoO_x_1 mM photoanodes also increased. This result confirms the presence of CoO_x and Al_2O_3 on the surface of the TZF photoanode. Additionally, the XPS result of Ti 2p of TZF and TZF/Al_2O_3/CoO_x_1 mM photoanodes is shown in Fig. 4D. It shows that there was not much difference in Ti 2p of both samples. The CoO_x layer on the TZF/Al_2O_3 for effective hole transport was prepared using different concentrations of the cobalt precursor solution (0.5, 1, and 5 mM), and the photocurrent densities of the obtained photoanodes were compared, as presented in Fig. S7.† The optimal concentration of the Co precursor solution is 1 mM, at which the TZF/Al_2O_3/CoO_x_1 mM photoanodes show the highest photocurrent density.

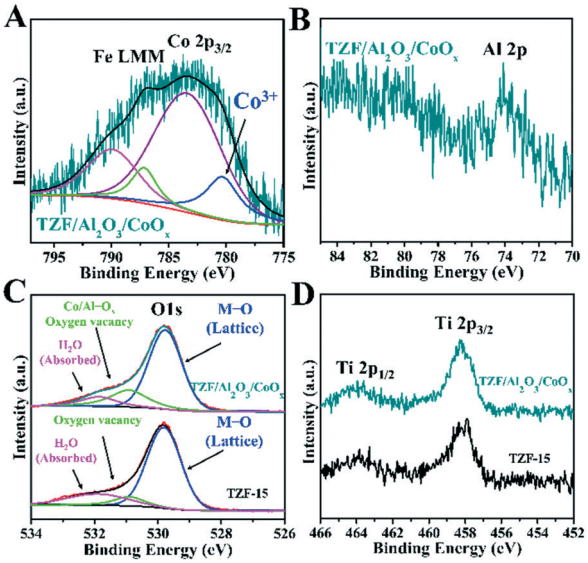

Fig. 4 XPS narrow scan spectra of (A) Co 2p, (B) Al 2p, (C) O 1s and (D) Ti 2p recorded from TZF-15 and TZF/Al_2O_3/CoO_x.

Fig. 5A shows the *J–V* curves of conventional pure ZFO, TZF, and TZF/Al_2O_3/CoO_x_1 mM photoanodes. The pure ZFO and TZF-15 photoanodes have photocurrent densities of 0.14 and 0.48 mA cm^{-2} at 1.23 V *vs.* RHE, whereas further modifying TZF-15 with the Al_2O_3 and CoO_x coating resulted in a dramatic increase to 0.73 mA cm^{-2} at 1.23 V *vs.* RHE. This is the highest photocurrent density and excellent stability for TZF NC coated with Al_2O_3/CoO_x photoanodes among those reported in the literature on $ZnFe_2O_4$ photoanodes, and the comparative results are shown in Table S5.† Moreover, the onset potential of the TZF/Al_2O_3/CoO_x_1 mM photoanode was cathodically shifted (0.83 to 0.77 V *vs.* RHE) compared to that of the TZF-15 photoanodes. Because of surface passivation using Al_2O_3 and CoO_x the surface defects on TZF will remove and should decrease the onset potential for water oxidation. Thus, Al_2O_3 should play a vital role in pull-out and storage of the photogenerated holes from the ZFO photoanode. Furthermore, CoO_x could effectively minimize the electrode–electrolyte interface charge transfer resistance by extracting holes from the photoanodes for water oxidation. Additionally, an apparent negative shift (relative to that of pure ZFO) in the photocurrent onset potential was observed for the TZF/Al_2O_3/CoO_x_1 mM photoanode, indicating that both Al_2O_3 and CoO_x could lower the water oxidation energy barrier for interfacial charge transfer in TZF[55] (see EIS data; Fig. 5B). This easy transfer of the

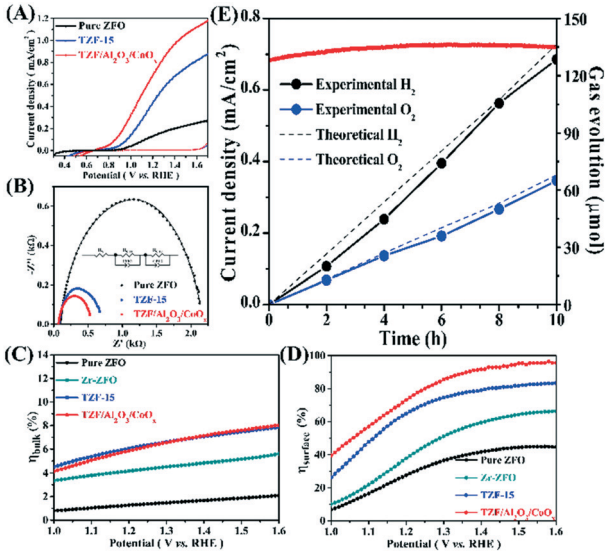

Fig. 5 (A) Photocurrent density *vs.* potential curves measured under 1 sun illumination (solid lines) and dark (dashed lines) conditions. (B) Nyquist plots measured under illumination at 1.23 V *vs.* RHE using 1 M NaOH for pure ZFO, TZF-15, and TZF/Al_2O_3/CoO_x photoanodes. The equivalent circuit used for EIS fitting is shown in Fig. 5B, inset; the evaluation of charge separation efficiency (C) in the bulk (η_{bulk}) and (D) on the surface ($\eta_{surface}$) for pure ZFO, Zr-ZFO, TZF-15, and TZF/Al_2O_3/CoO_x photoanodes with hole scavenger tests. (E) Amperometry (*J*–*t*) plot and corresponding hydrogen and oxygen evolution under 1 sun illumination in 1 M NaOH of TZF/Al_2O_3/CoO_x photoanodes.

photogenerated holes promotes charge separation and, thus, lowers the onset potential. Compared to the TZF photoanode, a sharp rise in the photocurrent density was detected beyond the onset potential and the tendency for saturation in the high potential region (>1.23 V *vs.* RHE) signposts the enhanced charge transfer in the photoanodes. Thus, the synergistic effects of Al_2O_3 and CoO_x result in significantly advanced PEC activity for water splitting compared with that of the pure TZF photoelectrodes. The results are similar to the results obtained by Fu *et al.* for $ZnWO_4$.[56] To verify the effects of the Al_2O_3/CoO_x passivation layer on the Zr-ZFO photoanodes, EIS measurements of the pure ZFO, TZF, and TZF/Al_2O_3/CoO_x_1 mM photoanodes were performed under 1 sun illumination. Fig. 5B shows typical EIS Nyquist plots fitted by an equivalent circuit model, and the results are listed in Table S6.† The drastically reduced semicircle radius for TZF/Al_2O_3/CoO_x_1 mM relative to those of pure ZFO and TZF suggests that the R_{CT2} of photogenerated holes is reduced from 120 to 108 Ω because of the high catalytic activities of Al_2O_3 and CoO_x. Thus, surface modification can promote charge separation at the electrode–electrolyte interface and enhance the oxygen evolution reaction (OER) kinetics. Fig. S8A† shows the ABPE spectra of the pure ZFO, TZF and TZF/Al_2O_3/CoO_x_1 mM photoanodes. The maximum ABPE value of 0.075% at 1.02 V *vs.* RHE was obtained for TZF/Al_2O_3/CoO_x_1 mM, which is approximately 7 times greater than that of pure ZFO. In Fig. S8B,† the MS plots show the charge carrier density (N_D) values of TZF, which exhibits a significantly increased N_D compared to pure ZFO because Zr and Ti had diffused into the ZFO lattice. Instead, there is not much difference in the N_D values derived from the slope after the Al_2O_3/CoO_x modification of TZF, indicating that the passivation layer did not affect the electrical properties of the photoanode lattice, but it did lower the onset potential of TZF for PEC water oxidation.[50] Moreover, the calculated electron transport times obtained from the IMPS analysis of each sample are summarized in Fig. S8C and Table S7.† The TZF/Al_2O_3/CoO_x_1 mM sample exhibited a shorter electron transport time of 424 μs than the other samples. This result indicates that another effect of the Al_2O_3/CoO_x modification is faster electron transport, which can contribute to enhanced surface charge transfer properties. The incident photon-to-current efficiency (IPCE) spectra are displayed within the wavelength region of 300–800 nm at 1.23 V *vs.* RHE, as shown in Fig. S8D.†[57,58] The IPCE spectra were measured at 1.23 V *vs.* RHE using a CS130 monochromator (Mmac-200, spectro) with a 300 W xenon arc lamp in the range from 300 nm to 800 nm. The IPCE was obtained using the following equation:[44]

$$\text{IPCE}\ (\%) = (1240 \times J_{photo}(\text{mA cm}^{-2}))/(I_{inc}(\text{mW cm}^{-2}) \times \lambda(\text{nm})) \quad (8)$$

where J_{photo}, I_{inc} and λ are the photocurrent density, the incident monochromatic light power density and the wavelength, respectively. The IPCE values of all as-prepared samples dropped to zero at a wavelength of 610 nm, which is related to the light absorption range of ZFO photoanodes. The maximum IPCE values are 1.49%, 6.69%, and 9.26% for pure ZFO, TZF, and TZF/Al_2O_3/CoO_x_1 mM, respectively. Overall this result suggests that Zr^{4+}/Ti^{4+} diffusion/doping and surface modification has a positive effect on the PEC splitting of water.

To assess the effects of various approaches (Zr^{4+}/Ti^{4+} diffusion/doping and Al_2O_3/CoO_x passivation), we tested the bulk and surface charge separation efficiencies of pure ZFO, Zr-ZFO, TZF, and TZF/Al_2O_3/CoO_x_1 mM photoanodes. Fig. S9† displays the *J*–*V* curves of pure ZFO, Zr-ZFO, TZF-15 and TZF/Al_2O_3/CoO_x_1 mM photoanodes in 1 M NaOH with and without 0.5 M H_2O_2 as a sacrificial donor. Fig. 5C and D show the bulk charge injection (η_{bulk}) and surface charge separation efficiencies ($\eta_{surface}$) of the pure ZFO, Zr-ZFO, TZF and TZF/Al_2O_3/CoO_x_1 mM photoanodes in 1 M NaOH with 0.5 M H_2O_2 as a sacrificial donor.[59] As shown in Fig. 5C pure ZFO, Zr-ZFO and TZF-15 exhibits the η_{bulk} values of 1.35%, 4.28% and 6.24% respectively. The η_{bulk} of TZF is 4.62 times that of the pure ZFO, which suggests that Zr^{4+} doping and Ti^{4+} diffusion in ZFO can further improve the electron–hole separation in TZF. The enhanced η_{bulk} in TZF is consistent with the increased charge carrier densities obtained by MS analysis. However, loading the Al_2O_3/CoO_x co-catalyst does not bring additional improvement in η_{bulk} of TZF-15. Additionally, the interfacial charge separation properties of the photoanodes were evaluated by calculating $\eta_{surface}$, as shown in Fig. 5D. The values of $\eta_{surface}$ are 30.60%, 42.14%,

68.53%, and 77.55% at 1.23 V *vs.* RHE for the pure ZFO, Zr-ZFO, TZF, and TZF/Al_2O_3/CoO_x_1 mM photoanodes, respectively. The increased $\eta_{surface}$ of TZF compared to that of the Zr-ZFO photoanode specifies that the diffused Zr^{4+} and Ti^{4+} had reached the top of the ZFO NCs, and they act as a passivation layer on the surface of ZFO in the form of TiO_2/ZrO_2. Thus, Zr^{4+} and Ti^{4+} refine the ZFO–electrolyte interface because of the suppressed surface recombination. Moreover, the TZF/Al_2O_3/CoO_x_1 mM photoanodes exhibited significantly higher interfacial charge separation efficiencies of up to 96.46% (at 1.58 V *vs.* RHE), which directs that charge recombination can be greatly suppressed by the Al_2O_3 and CoO_x layers. The charge separation efficiency results are also supported by the decreased R_{CT1} and R_{CT2} values obtained in the EIS measurements (Fig. 5B).

The stability of the TZF/Al_2O_3/CoO_x_1 mM photoanode was assessed during the PEC water splitting reaction, and a specially designed three-armed PEC reactor was used for this reaction. The amounts of hydrogen/oxygen (H_2/O_2) gases evolved over the TZF/Al_2O_3/CoO_x_1 mM photoanodes (1.0 × 1.0 cm^2) under 100 mW cm^{-2} light illumination (at 1.23 V *vs.* RHE) were measured by gas chromatography. The hydrogen (H_2) and oxygen (O_2) evolution was accompanied by a slightly increased current density, as shown in the chronoamperometry plots in Fig. 5E (red line). Fig. 5E shows that both (H_2/O_2) gases were evolved linearly with time.[60]

At the TZF/Al_2O_3/CoO_x_1 mM photoanode:

$$2H_2O(TZF/Al_2O_3/CoO_x + h\nu \rightarrow O_2(g) + 4H^+ + 4e^-) \quad (9)$$

At the Pt counter electrode:

$$4H^+ + 4e^- \rightarrow 2H_2(g) \quad (10)$$

After 10 h of illumination, 65 and 130 μmol of O_2 and H_2 were evolved, respectively. Moreover, the TZF/Al_2O_3/CoO_x_1 mM photoanode showed excellent stability for water splitting during 10 h under continuous illumination. This result shows the photostability of the TZF/Al_2O_3/CoO_x_1 mM electrode during the PEC water splitting.

Based on the analytical results, a schematic of the charge separation and transfer in the bulk and photoanode/electrolyte interface of the TZF/Al_2O_3/CoO_x_1 mM photoanode during PEC water splitting is shown in Fig. 6. In addition to the suppression of electron back injection from FTO to the Zr-ZFO lattice, the TiO_2 underlayer induces the self-diffusion of Ti^{4+} from the TiO_2 underlayer into the Zr-ZFO lattice during high-temperature quenching. Thus, both the suppression of back injection and the diffusion of Ti^{4+} during high-temperature quenching seem to be the reasons for the improved charge transfer and, thus, improved PEC performance in Zr-ZFO photoanodes were modified with a TiO_2 underlayer. Thus, under illumination, the amount of photogenerated electrons and holes in the ZFO NCs are quickly moved toward the substrates through the semiconductor bulk and, ultimately, to the Pt counter electrode for water reduction; simultaneously, the photogenerated holes move to the surface of the photoelectrode and are trapped by the ZrO_2/TiO_2 layer.

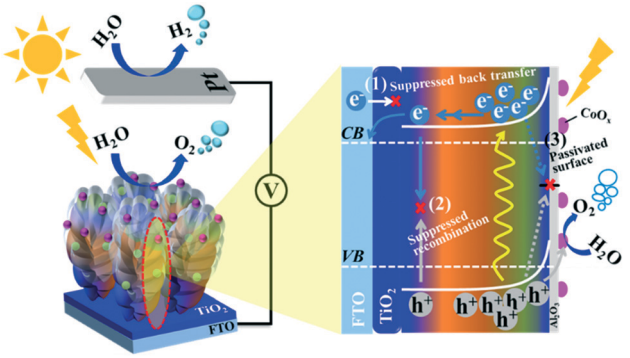

Fig. 6 Schematic diagram of photoelectrochemical hydrogen production by water splitting and corresponding charge transfer mechanism in Ti^{4+}/Zr^{4+} diffusion/doping and surface crowned TZF/Al_2O_3/CoO_x photoanode.

In the present system, because of the higher number of recombination centres in the bulk and surface of the Zr-ZFO photoanode, we observed less photogenerated hole transfer at the electrode–electrolyte interface, which reduced the water oxidation kinetics. On the other hand, Zr^{4+} and Ti^{4+} diffusion/doping effectively increased the electron donor density and enhanced the PEC performance of TZF-15 (Fig. 6, magnified view). However, after the modification of TZF with Al_2O_3, the photogenerated holes in the photoanode were stored temporarily in Al_2O_3.[49] Thus the presence of Al_2O_3 can effectively transfer the photogenerated holes for the OER and prevent the back reaction.[61] After modification on the surface of the TZF photoanode with Al_2O_3 and CoO_x, the trapped holes in the Al_2O_3 layer could be extracted by the CoO_x cocatalyst. Thus, the prepared photoanodes revealed a cathodic shift in the photocurrent onset potential and lower surface charge recombinations than the TZF-15 photoanode. Additionally, the Mott–Schottky results show no significant difference in the N_D of TZF after Al_2O_3/CoO_x modification, but the charge recombination in the bulk was strongly inhibited which enhanced the charge separation efficiencies (η_{bulk} and $\eta_{surface}$) remarkably. Further, the introduction of Al_2O_3/CoO_x on the TZF NCs led to the cathodic shift in the *J*–*V* measurements and reduced the interface resistance at the photoanode/electrolyte junction, suggesting that the hole transfer and surface passivation catalytic behavior of Al_2O_3 and CoO_x are beneficial for efficient PEC water oxidation.

4. Conclusions

In summary, we have demonstrated the Ti diffusion and surface modification of *in situ* Zr-doped zinc ferrite nanocoral photoanodes for PEC water splitting. By varying the precursor TiO_2 solution concentration, we optimized the compact TiO_2 underlayers. The influence of the Ti^{4+} diffusion/doping and TiO_2/ZrO_2 surface passivation of the TZF nanocorals during the

high-temperature quenching was demonstrated by a significantly negative onset potential and superior photocurrent density. The Ti^{4+}/Zr^{4+} diffusion/doping and TiO_2/ZrO_2 passivation strategy in TZF reduces the recombination both in the bulk and on the surface, which effectively enhances the PEC water oxidation performance. TZF/Al_2O_3/CoO_x_1 mM photoanodes exhibited significantly higher surface charge separation efficiencies of 77.55% (at 1.23 V *vs.* RHE), suggesting that charge recombination can be greatly suppressed by the Al_2O_3/CoO_x. Compared to conventional ZFO nanorods (0.14 mA cm^{-2} at 1.23 V *vs.* RHE), the TZF/Al_2O_3/CoO_x_1 mM photoanode showed a 421% increase in photocurrent density. The amount of evolved O_2 and H_2 reached 65 and 130 μmol, respectively, after 10 h over highly stable TZF/Al_2O_3/CoO_x_1 mM. We believe that our design and strategy of TZF is a useful approach for developing novel photocatalysts for PEC water splitting.

Conflicts of interest

There are no conflicts to declare.

Acknowledgements

This research was supported by the Brain Pool Program through the National Research Foundation of Korea (NRF) funded by the Ministry of Science and ICT (2017H1D3A1A02014020). This work was also supported by the National Research Foundation of Korea (NRF) grant funded by the Korea government (MSIT) (2018R1D1A1B07043453 and 2019R1A2C1006402).

Notes and references

1 J. Zheng, H. Zhou, Y. Zou, R. Wang, Y. Lyu, S. P. Jiang and S. Wang, *Energy Environ. Sci.*, 2019, **12**, 2345–2374.
2 A. Fujishima and K. Honda, *Nature*, 1972, **238**, 37–38.
3 A. Kudo and Y. Miseki, *Chem. Soc. Rev.*, 2009, **38**, 253–278.
4 T. Hisatomi, J. Kubota and K. Domen, *Chem. Soc. Rev.*, 2014, **43**, 7520–7535.
5 C. Y. Lee, A. C. Taylor, S. Beirne and G. G. Wallace, *Adv. Energy Mater.*, 2017, **7**, 1701060.
6 K. Sivula, R. Zboril, F. L. Formal, R. Robert, A. Weidenkaff, J. Tucek, J. Frydrych and M. Gratzel, *J. Am. Chem. Soc.*, 2010, **132**, 7436–7444.
7 R. Franking, L. Li, M. A. Lukowski, F. Meng, Y. Tan, R. J. Hamers and S. Jin, *Energy Environ. Sci.*, 2013, **6**, 500–512.
8 K. Sivula and R. Krol, *Nat. Rev. Mater.*, 2016, **1**, 16010.
9 A. G. Hufnagel, K. Peters, A. Müller, C. Scheu, D. Fattakhova-Rohlfing and T. Bein, *Adv. Funct. Mater.*, 2016, **26**, 4435–4443.
10 N. Guijarro, P. Bornoz, M. Prévot, X. Yu, X. Zhu, M. Johnson, X. Jeanbourquin, F. Le Formal and K. Sivula, *Sustainable Energy Fuels*, 2018, **2**, 103–117.
11 X. Zhu, N. Guijarro, Y. Liu, P. Schouwink, R. A. Wells, F. Le Formal, S. Sun, C. Gao and K. Sivula, *Adv. Mater.*, 2018, **30**, 1801612.
12 A. Polo, C. R. Lhermitte, M. V. Dozzi, E. Selli and K. Sivula, *Surfaces*, 2020, **3**, 93–104.
13 Y. Lan, Z. Liu, Z. Guo, M. Ruan and Y. Xin, *J. Colloid Interface Sci.*, 2019, **552**, 111–121.
14 P. F. Teh, S. S. Pramana, Y. Sharma, Y. W. Ko and S. Madhavi, *ACS Appl. Mater. Interfaces*, 2013, **5**, 5461–5467.
15 M. V. Reddy, C. Y. Quan, K. W. Teo, L. J. Ho and B. V. R. Chowdari, *J. Phys. Chem. C*, 2015, **119**, 4709–4718.
16 Y. N. NuLi, Y. Q. Chu and Q. Z. Qin, *J. Electrochem. Soc.*, 2004, **151**, A1077–A1083.
17 J. H. Kim, J. H. Kim, J. H. Kim, Y. K. Kim and J. S. Lee, *Sol. RRL*, 2020, **4**, 1900328.
18 Y. Guo, N. Zhang, X. Wang, Q. Qian, S. Zhang, Z. Li and Z. Zou, *J. Mater. Chem. A*, 2017, **5**, 7571–7577.
19 T. Hisatomi, H. Dotan, M. Stefik, K. Sivula, A. Rothschild, M. Gratzel and N. Mathews, *Adv. Mater.*, 2012, **24**, 2699–2702.
20 L. Steier, I. Herraiz-Cardona, S. Gimenez, F. Fabregat-Santiago, J. Bisquert, S. D. Tilley and M. Grätzel, *Adv. Funct. Mater.*, 2014, **24**, 7681–7688.
21 T. Hisatomi, J. Brillet, M. Cornuz, F. Le Formal, N. Tetreault, K. Sivula and M. Gratzel, *Faraday Discuss.*, 2012, **155**, 223–232.
22 F. Le Formal, M. Grätzel and K. Sivula, *Adv. Funct. Mater.*, 2010, **20**, 1099–1107.
23 O. Zandi, J. A. Beardslee and T. Hamann, *J. Phys. Chem. C*, 2014, **118**, 16494–16503.
24 J. Kim, Y. Jang, J. Kim, J. Jang, S. Choi and J. Lee, *Nanoscale*, 2015, **7**, 19144–19151.
25 K. T. Chen, H. Y. Chen and C. J. Tsai, *Electrochim. Acta*, 2019, **319**, 577–586.
26 S. Kim, M. A. Mahadik, W. S. Chae, J. Ryu, S. H. Choi and J. S. Jang, *Appl. Surf. Sci.*, 2020, **513**, 145528.
27 R. H. Misho and W. A. Murad, *Sol. Energy Mater. Sol. Cells*, 1992, **27**, 335–345.
28 B. Ravel and M. Newville, *J. Synchrotron Radiat.*, 2005, **12**, 537–541.
29 J. R. Lakowicz, *Principles of fluorescence spectroscopy*, Springer, New York, 2006.
30 T. W. Kim and K. S. Choi, *Science*, 2014, **343**, 990–994.
31 M. A. Mahadik, P. S. Shinde, M. Cho and J. S. Jang, *J. Mater. Chem. A*, 2015, **3**, 23597–23606.
32 C. D. Wagner, W. M. Riggs, L. E. Davis and J. F. Moulder, *Handbook Of X-Ray Photoelectron Spectroscopy*, ed. G. E. Mullenberg, Perkin-Elmer Corporation Press, Minnesota, 1979, vol. 2, p. 100.
33 A. Bumajdad, A. A. Nazeer, F. A. Sagheer, S. Nahar and M. I. Zaki, *Sci. Rep.*, 2018, **8**, 1–9.
34 M. Rioult, H. Magnan, D. Stanescu and A. Barbier, *J. Phys. Chem. C*, 2014, **118**, 3007–3014.
35 D. Cao, W. Luo, J. Feng, X. Zhao, Z. Lia and Z. Zou, *Energy Environ. Sci.*, 2014, **7**, 752–759.
36 Z. P. Chen, W. Q. Fang, B. Zhang and H. G. Yang, *J. Alloys Compd.*, 2013, **550**, 348–352.
37 Y. Hou, X. Y. Li, Q. D. Zhao, X. Quan and G.-H. Chen, *Adv. Funct. Mater.*, 2010, **20**, 2165–2174.
38 L. Hou, H. Hua, L. Lian, H. Cao, S. Zhu and C. Yuan, *Chem. – Eur. J.*, 2015, **21**, 13012–13019.

39 S. Wang, T. He, J. H. Yun, Y. Hu, M. Xiao and A. Du, *Adv. Funct. Mater.*, 2018, **28**, 1802685.
40 H. Song, L. Zhu, Y. Li, Z. Lou, M. Xiao and Z. Ye, *J. Mater. Chem. A*, 2015, **3**, 8353–8360.
41 X. Zhou, X. Li, H. Sun, P. Sun, X. Liang, F. Liu, X. Hu and G. Lu, *ACS Appl. Mater. Interfaces*, 2015, **7**, 15414–15421.
42 P. Liao, M. C. Toroker and E. A. Carter, *Nano Lett.*, 2011, **11**, 1775–1781.
43 A. G. Tamirat, W. N. Su, A. A. Dubale, H. M. Chen and B. J. Hwang, *J. Mater. Chem. A*, 2015, **3**, 5949–5961.
44 G. Liu, S. Ye, P. Yan, F. Xiong, P. Fu, Z. Wang, Z. Chen, J. Shi and C. Li, *Energy Environ. Sci.*, 2016, **9**, 1327–1334.
45 X. Yu, P. Yang, S. Chen, M. Zhang and G. Shi, *Adv. Energy Mater.*, 2017, **7**, 1601805.
46 G. M. Wang, Y. C. Ling, D. A. Wheeler, K. E. N. George, K. Horsley, C. Heske, J. Z. Zhang and Y. Li, *Nano Lett.*, 2011, **11**, 3503–3509.
47 A. Hassan, X. Zhang, X. Liu, C. E. Rowland, A. M. Jawaid, S. Chattopadhyay, A. Gulec, A. Shamirian, X. Zuo, R. F. Klie and R. D. Schaller, *ACS Nano*, 2017, **11**, 10070–10076.
48 Y. F. Xu, X. D. Wang, H. Y. Chen, D. B. Kuang and C. Y. Su, *Adv. Funct. Mater.*, 2016, **26**, 4414–4421.
49 Y. Yang, M. Forster, Y. Ling, G. Wang, T. Zhai, Y. Tong, A. J. Cowan and Y. Li, *Angew. Chem., Int. Ed.*, 2016, **55**, 3403–3407.
50 A. Annamalai, P. S. Shinde, A. Subramanian, J. Y. Kim, J. H. Kim, S. H. Choi, J. S. Lee and J. S. Jang, *J. Mater. Chem. A*, 2015, **3**, 5007–5013.
51 J. Su, L. Guo, N. Bao and C. A. Grimes, *Nano Lett.*, 2011, **11**, 1928–1933.
52 Z. Liu, L. Wang, X. Yu, J. Zhang, R. Yang, X. Zhang, Y. Ji, M. Wu, L. Deng, L. Li and Z. L. Wang, *Adv. Funct. Mater.*, 2019, **29**, 1807279.
53 M. A. Mahadik, A. Subramanian, H. S. Chung, M. Cho and J. S. Jang, *ChemSusChem*, 2017, **10**, 2030–2039.
54 X. Zhang, Y. S. Chen, P. V. Kamat and S. Ptasinska, *J. Phys. Chem. C*, 2018, **122**, 13894–13901.
55 T. K. Sahu, A. K. Shah, G. Gogoi, A. S. Patra, M. S. Ansari and M. Qureshi, *Chem. Commun.*, 2018, **54**, 10483–10486.
56 S. Fu, H. Hu, C. Feng, Y. Zhang and Y. Bi, *J. Mater. Chem. A*, 2019, **7**, 2513–2517.
57 J. H. J. Wijten, R. P. H. Jong, G. Mul and B. M. Weckhuysen, *ChemSusChem*, 2018, **11**, 1374–1381.
58 H. Y. Hafeez, S. K. Lakhera, N. Narayanan, S. Harish, Y. Hayakawa, B. K. Lee and B. Neppolian, *ACS Omega*, 2019, **4**, 880–891.
59 H. Dotan, K. Sivula, M. Gratzel, A. Rothschild and S. C. Warren, *Energy Environ. Sci.*, 2011, **4**, 958–964.
60 L. Zhang, T. Wei, J. Yue, L. Sheng, Z. Jiang, D. Yang, L. Yuan and Z. Fan, *J. Mater. Chem. A*, 2017, **5**, 11188–11196.
61 Z. Fan, Z. Xu, S. Yan and Z. Zou, *J. Mater. Chem. A*, 2017, **5**, 8402–8407.

